



OPEN

Evolution of microstructure, strain and physical properties in oxide nanocomposite films

SUBJECT AREAS:
ELECTRONIC PROPERTIES
AND MATERIALS
COMPOSITESAiping Chen¹, Marcus Weigand¹, Zhenxing Bi¹, Wenrui Zhang², Xuejie Lü¹, Paul Dowden¹,
Judith L. MacManus-Driscoll³, Haiyan Wang² & Quanxi Jia¹Received
24 March 2014Accepted
21 May 2014Published
24 June 2014Correspondence and
requests for materials
should be addressed to
A.P.C. (apchen@lanl.
gov) or Q.X.J. (qxjia@
lanl.gov)¹Center for Integrated Nanotechnologies (CINT), Los Alamos National Laboratory, Los Alamos, NM 87545 (USA), ²Department of Electrical and Computer Engineering, Texas A&M University, College Station, TX 77843-3128 (USA), ³Department of Materials Science and Metallurgy, University of Cambridge, Pembroke Street, Cambridge, CB2 3QZ (UK).

We, using LSMO:ZnO nanocomposite films as a model system, have studied the effect of film thickness on the physical properties of nanocomposites. It shows that strain, microstructure, as well as magnetoresistance strongly rely on film thickness. The magnetotransport properties have been fitted by a modified parallel connection channel model, which is in agreement with the microstructure evolution as a function of film thickness in nanocomposite films on sapphire substrates. The strain analysis indicates that the variation of physical properties in nanocomposite films on LAO is dominated by strain effect. These results confirm the critical role of film thickness on microstructures, strain states, and functionalities. It further shows that one can use film thickness as a key parameter to design nanocomposites with optimum functionalities.

Extensive efforts have been devoted to explore technological applications and to understand fundamental physics in complex metal-oxides owing to their remarkable physical phenomena such as high temperature superconductivity¹, single-phase multiferroics^{2–4}, and colossal magnetoresistance^{5,6}. Artificially constructed horizontal oxide heterointerfaces in the form of superlattices, multilayers, and/or heterostructures have been widely investigated to manipulate physical properties^{7–9}. Recently, nanocomposites with a vertical interface network are emerging as an alternative approach to tune physical properties since microstructure, interfacial coupling, and lattice strain can be tailored from 2D to 3D^{10–19}. The lack of substrate clamping effect and the presence of large interfacial area in thick vertically aligned nanocomposite films in comparison with conventional horizontal heterostructures make such a new 3D architecture attractive²⁰ to tune the functionalities of materials²¹. Experimentally, multiferroics and magnetoelectric couplings have been demonstrated in nanocomposite thin films consisting of ferromagnetic and ferroelectric oxides (e.g., BaTiO₃:CoFe₂O₄, Pb(Zr_{0.52}Ti_{0.48})O₃-NiFe₂O₄, BiFeO₃:CoFe₂O₄)^{22–26}. In addition, the vertical interface in composite films can show both enhanced electronic and ionic conductivities, which could be used for fast ion conducting channels in solid-oxide fuel cells^{27,28}. Moreover, stress-mediated magnetic anisotropy has been observed in epitaxial ferromagnetic nanocomposites such as BiFeO₃:CoFe₂O₄, PbTiO₃:CoFe₂O₄ and BiFeO₃:La_{0.7}Sr_{0.3}MnO₃ (LSMO)^{29–31}. Another fascinating aspect is that the dynamic control of functionalities in these nanocomposites can be achieved through external stimuli such as applied stress or magnetic or electric fields^{32,33}. In order to achieve desired functionalities or tune physical properties of materials, the role of strain and microstructure on the functionality needs to be systematically investigated.

Among all the factors, film thickness plays an important role in controlling film microstructure, strain, and resulted film functionality. In single-phase oxide films, for instance, grain size, strain, and microstructure vary with thickness^{34,35}. The structural, optical, and magnetic properties can be also tuned by film thickness^{36–38}. However most of the previous studies on heteroepitaxial oxide nanocomposite films focus on varying phase compositions^{39,40}, substrate orientations^{24,41}, material systems^{14,42–44}, substrate lattice parameter and symmetry^{11,29,45,46}, etc. The thickness effect, a key factor in composite films, is rarely studied. Such understanding could be critical for the design of nanocomposite with optimized functionalities. In this work, we vary the film thickness of LSMO:ZnO nanocomposite films to explore its role on the overall film microstructure and strain as well as the resulted magnetoresistance properties of the composite films. Furthermore, different substrates (*r*-



plane sapphire, *c*-plane sapphire, and LaAlO₃) were used and the film thickness was varied from 10 nm to 200 nm. This work could reveal the strain and microstructure evolution as a function of film thickness and, in turn, provide important design guideline for nanocomposites with desired functionalities.

Results

Structural characterization of nanocomposites. The structures of nanocomposite films with different film thicknesses on various substrates have been analyzed by X-ray diffraction (XRD). As shown in Figure 1a, except for the substrate peaks, only LSMO (111) and ZnO (002) peaks were observed in the typical θ - 2θ scans, indicating that LSMO:ZnO nanocomposite films on *c*-plane sapphire are preferentially oriented. On the other hand, Figure 1b shows that the LSMO phase on *r*-plane sapphire has two sets of peaks, i.e., (00 l) and (0 l l). Figure 1c shows that the strain state of LSMO phase in these films on both *c*- and *r*-plane sapphires is independent of the film thickness since their lattice parameters are the same as the bulk values. Figure 1d represents the XRD of LSMO:ZnO nanocomposite films on LAO (001) substrates. It is noted that both LSMO and ZnO phases are preferentially oriented out-of-plane. The Φ -scans of LSMO {202} and LAO {202} show a fourfold symmetry (Figure 1e), suggesting that the LSMO phase on the LAO substrate is epitaxially grown (cube-on-cube). The appearance of four peaks of ZnO {112} is from the two variants of {112} with 90° in-plane rotation (see Figures S1a and S1b). Detailed analysis shows that the *c*-axis of ZnO aligned along LAO [110] and [110] in-plane. The orientation relationship of films on LAO is determined to be (001)_{LSMO}|| (110)_{ZnO}|| (001)_{LAO}, [110]_{LSMO}|| [001]_{ZnO}|| [110]_{LAO} and [110]_{LSMO}|| [001]_{ZnO}|| [110]_{LAO}. Different from the films on sapphire substrates, the out-of-plane lattice constant of films on LAO (001) strongly depends on film thickness. The LSMO (002) peak monotonically shifts to the larger angles with increasing film thickness (Figure S1c), indicating that

the strain varies with the film thickness. Figure 1f shows that the LSMO (002) lattice spacing decreases from 1.99 Å to 1.95 Å with increase of the film thickness from 10 nm to 200 nm. It is noted that the LSMO phase is still strained even at a film thickness of 200 nm. When the nanocomposite films are thin enough, the strain in the LSMO phase is controlled by the LAO substrate. However, the strain of LSMO phase is dominated by the secondary ZnO phase when the films become thicker (200 nm). It has been reported that a vertical domain matching of 5 LSMO lattice spacings along [001] with 6 ZnO lattice spacings along [110] can generate a vertical strain in LSMO phase in thick films^{20,21,40}.

Microstructural characterization of nanocomposites. To investigate the thickness dependent microstructures of the composite films, transmission electron microscopy (TEM) and scanning TEM (STEM) in high-angle annular dark-field (HAADF) mode were conducted. Since the recorded intensity in STEM-HAADF is proportional to Z^n ($n = 1.5 \sim 2$), the LSMO and ZnO phases can be easily identified as bright and dark contrast areas because of their very different *Z* numbers. Figure 2a shows a plan-view STEM image of the 20 nm LSMO:ZnO film on *r*-plane sapphire. It reveals that the nanocomposite consists of circular nano-islands with a few tens of nanometers in diameter separated by boundaries. Indeed, the STEM-EDX line scan reveals that the LSMO circular grains are embedded in the ZnO matrix (Figures S2a and S2b). Thus, high density of grain boundaries (GBs) and phase boundaries can be expected in this thin sample due to the smaller grains. Figure 2b shows a STEM image of this nanocomposite with a 200 nm thickness. The dark areas represent the ZnO phase and the bright regions are the LSMO phase, which is further confirmed by the STEM-EDX line scan (Figures S2c and S2d). The microstructure of this thick sample is quite different from the thin sample. It is interesting that the ZnO nanopillars tend to embed in the LSMO matrix. The LSMO phase is connected into much larger domains. Thus, the 20 nm nanocomposite film on *r*-plane sapphire consists of nanograins with high

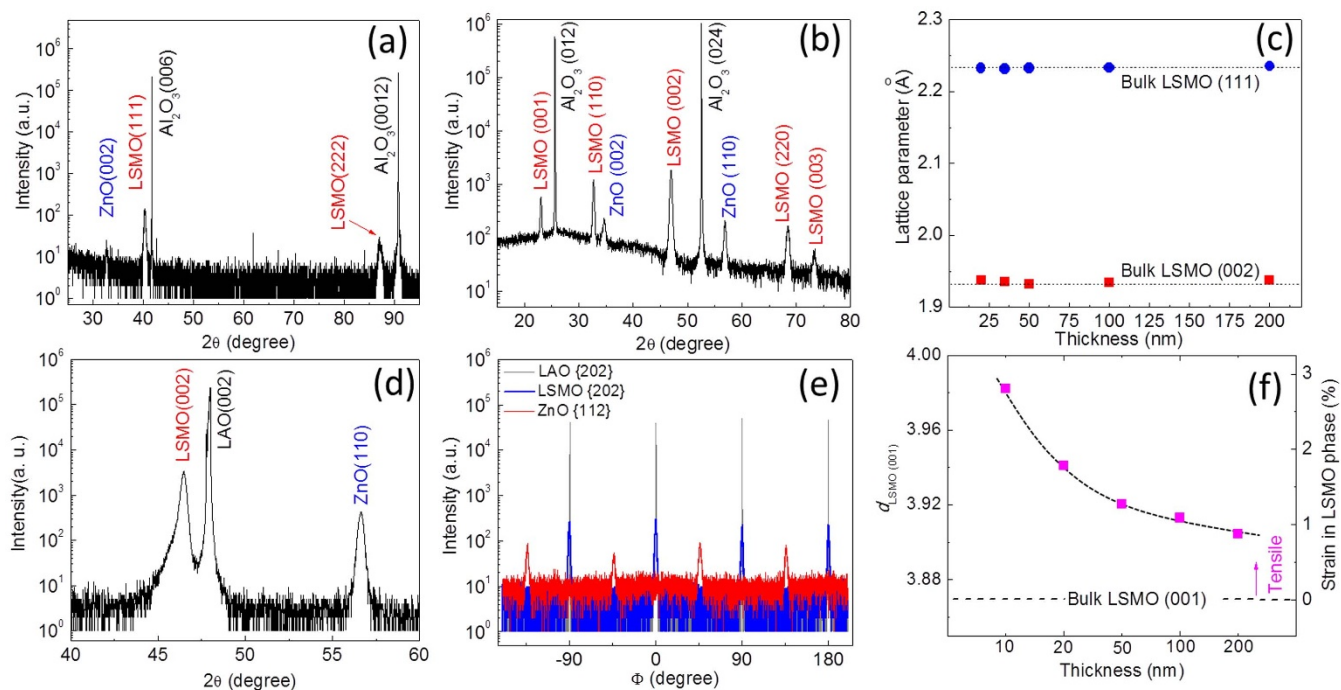


Figure 1 | XRD of the nanocomposite films on different substrates. (a) XRD (θ - 2θ) scan of LSMO:ZnO nanocomposites on *c*-sapphire substrates. (b) XRD (θ - 2θ) scan of LSMO:ZnO nanocomposites on *r*-plane sapphire substrates. (c) Thickness dependent lattice parameters of the LSMO phase grown on *c*- and *r*-plane sapphire substrates. (d) The XRD pattern of LSMO:ZnO nanocomposite films deposited on LAO (001) substrates. (e) Φ -scans of LAO {202}, LSMO {202} and ZnO {112}. (f) Thickness dependent strain (lattice parameter) of the nanocomposite films grown on LAO substrates. PDF#51-0409 is used for bulk LSMO reference. Pseudocubic structure rather than Rhombohedral structure is used in this work for simplicity.

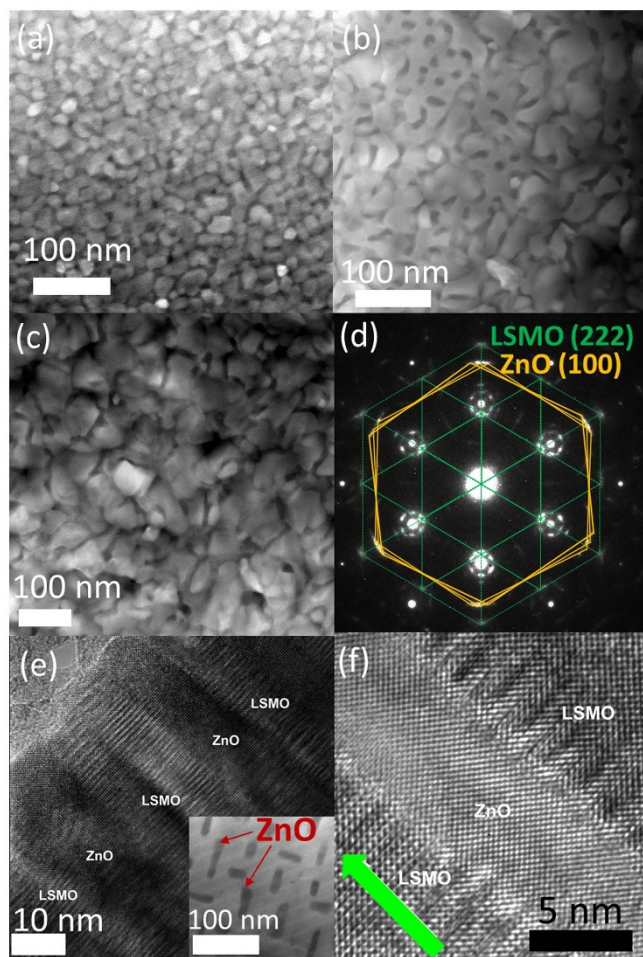


Figure 2 | Microstructures of nanocomposites on different substrates. (a) Plan-view STEM image of 20 nm LSMO:ZnO film on *r*-plane sapphire. (b) Plan-view STEM image of the 200 nm LSMO:ZnO film on *r*-plane sapphire. (c) Plan-view STEM image of the 200 nm LSMO:ZnO film on *c*-plane sapphire. (d) Electron diffraction of a 200 nm film on *c*-plane sapphire. (e) Low magnification cross-section TEM image of the 50 nm LSMO:ZnO film on LAO (001). Inset of (e) is the plan-view STEM image of nanocomposites on LAO (001). (f) HRTEM image of (e) with vertical interface between ZnO and LSMO phases.

density of GBs. Nevertheless, the LSMO grains grow bigger and connect with each other as a matrix when the film is getting thicker, resulting in a dramatically reduced GB density. The variation of microstructure with film thickness can greatly affect the magnetotransport and magnetoresistance (MR) of the LSMO phase. Figure 2c shows a plan-view STEM image of the 200 nm LSMO:ZnO nanostructures on *c*-plane sapphire. It is clearly seen that this nanocomposite film displays a granular structure with a few tens of nanometers in diameter of LSMO grains. The sample with a thickness of 20 nm on *c*-plane sapphire exhibits similar circular grains (Figure S3). It suggests that the nanocomposites on *c*-plane sapphire exhibit high density of GBs. The selected area diffraction (SAD) pattern, as shown in Figure 2d, shows an interesting in-plane matching when the nanocomposite films are on *c*-plane sapphire substrates. The LSMO phase has two different matching scenarios. The first one is the stack of LSMO (111) plane on Al_2O_3 (0001) plane (Figures S4a and S4b). The other one is the center of each hexagon consisting of 6 LSMO (111) planes overlapping with each substrate hexagon center (Figures S4c–S4e). The arc of diffraction from ZnO indicates that the ZnO phase exhibits a slight in-plane misalignment. Although the nanocomposite films grown on

c-plane sapphire have a preferential texture out-of-plane, the complex in-plane alignments result in a granular structure with high density of GBs, which do not strongly depend on film thickness. The microstructures of LSMO:ZnO nanocomposites on LAO (001) are shown in Figure 2e and 2f. It is interesting to note that both LSMO and ZnO nanodomains are vertically and alternatively aligned on the LAO substrate with a uniform feature size through the film thickness (Figure 2e). The plan-view STEM image, as shown in the inset of Figure 2e, further reveals that the ZnO rectangular nanopillars are embedded in the LSMO matrix (Figure S5). These perpendicular ZnO domains are consistent with the Φ -scan results in Figure 1e. Figure 2f shows a sharp LSMO/ZnO vertical interface with a ZnO feature size of ~ 8 nm. Detailed analysis also shows that the microstructure of nanocomposite LSMO:ZnO films on LAO is independent of film thickness.

Magnetotransport of nanocomposites. To reveal the property-structure correlation in these composite films, the magnetotransport and MR have been investigated at different temperatures and magnetic fields. Figure 3a shows the zero field resistance (normalized by their respective values at 340 K) of the nanocomposite films grown on *r*-plane sapphire with different thicknesses. The temperature at maximum resistance corresponds to the metal-insulator transition temperature (T_{MI}). It is obvious that the T_{MI} gradually shifts to lower temperatures and $R(T)/R(340\text{ K})$ values dramatically increase at low temperatures as the film thickness decreases. In comparison, the $R(T)/R(340\text{ K})$ curves of the nanocomposite films grown on *c*-plane sapphire with different thicknesses are shown in Figure 3b. It is interesting to note that the T_{MI} of these samples is almost independent of film thickness. The $R(T)/R(360\text{ K})$ values of nanocomposite films on LAO (001) are shown in Figure 3c. The T_{MI} decreases with reducing film thickness, which is also consistent with the trend of Curie temperature (T_C) (Figure S6). The 10 nm nanocomposite film displays a semiconductor-like behavior with no obvious metal-insulator transition (MIT). It should be noted that an accurate measurement of T_C of the 10 nm film from $M\sim H$ curves is challenging since the magnetic signal is quite weak (not shown here). Our results can be explained by the increase of Mn-O-Mn distance and the decrease of overlapping between the $3d$ -orbitals of Mn and $2p$ -orbitals of oxygen, induced by the large tensile strain of $\sim 2.8\%$ (Figure 1f)³⁹. The thicker films, however, exhibit MIT and T_{MI} increases with the increase of the film thickness. The T_{MI} of films on both *r*- and *c*-plane sapphire substrates as a function of film thickness is summarized in Figure 3d. The T_{MI} of nanocomposite films on *r*-plane sapphire increases from ~ 210 K to ~ 300 K with increasing the film thickness from 20 nm to 200 nm before reaching a plateau. Interestingly, the T_{MI} of nanocomposite films on *c*-plane sapphire is ~ 200 K and independent of film thickness. The T_{MI} also increases slightly with film thickness for the films on LAO substrates. Figure 2e shows the zero field resistivity at 20 K of these nanocomposite films with different thicknesses. These very thin films (10–20 nm) exhibit similar resistivity ($\sim 1\ \Omega\ \text{cm}$) regardless of substrates. Although the resistivity decreases with increasing film thickness in all films, their detailed behaviors are quite different. The resistivity of nanocomposite films on *c*-plane sapphire drops slowly with film thickness, while the resistivity of nanocomposite films on *r*-plane sapphire and LAO (001) decrease significantly (two orders of magnitude) from 20 to 50 nm. These results show that the 50 nm film on *c*-plane sapphire exhibits much higher resistivity than those on either *r*-plane sapphire or LAO with the same thickness. As these films on *r*- and *c*-plane sapphire substrates were deposited under the same deposition conditions except for the growth durations, the effect of oxygen content on the transport properties can be ruled out. Additionally, the lattice parameters of the films are independent of film thickness as shown in Figure 1c. It suggests

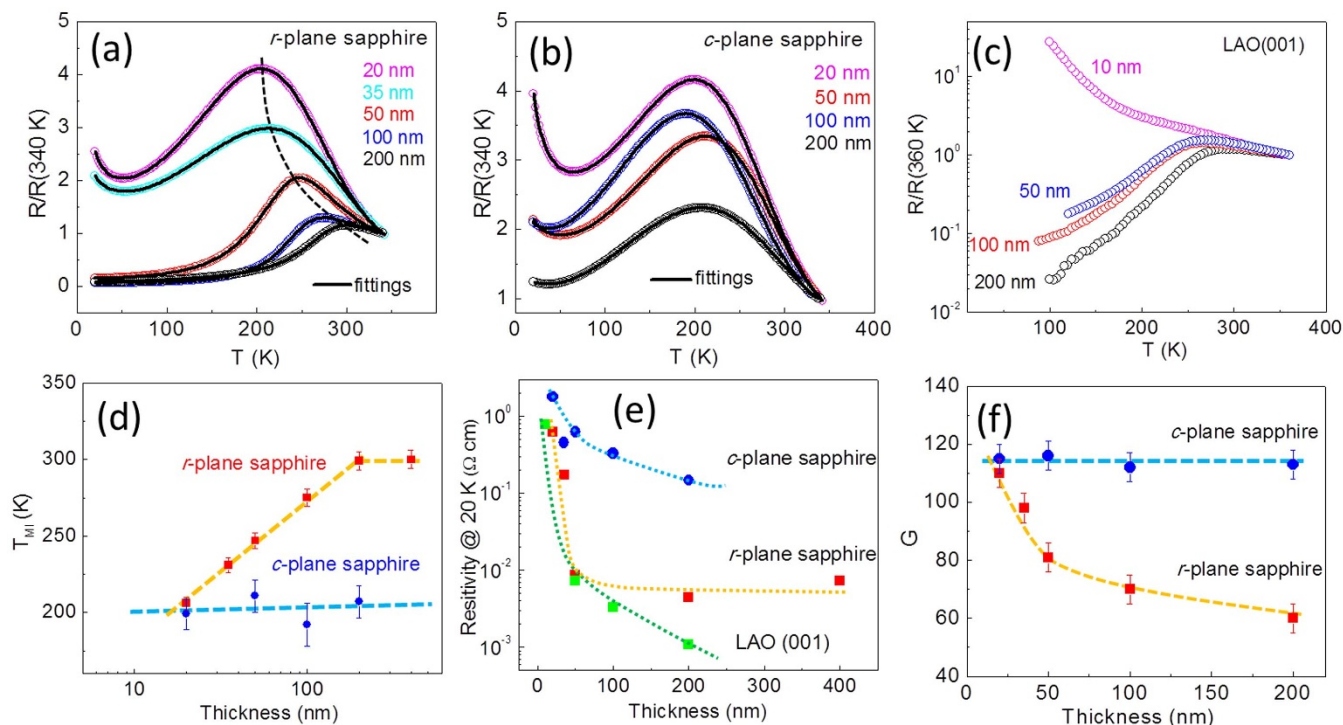


Figure 3 | Magnetotransport of nanocomposite films grown on *c*- and *r*-plane sapphires and LAO substrates. (a) and (b) Temperature dependence of normalized resistance in nanocomposite films deposited on *r*- and *c*-plane sapphire substrates, respectively. Solid curves are the fittings by equations [1] and [2]. The dashed line in (a) is used to guide the eye and shows the trend of T_{MI} . (c) Temperature dependence of normalized resistance in nanocomposite films deposited on LAO (001). (d) T_{MI} vs. film thickness. (e) resistivity vs. film thickness at 20 K. (f) G vs. film thickness.

the strain effect is not likely to be responsible for the variation of the transport properties. Thus, the microstructure evaluation with the film thickness should be the dominating factor in determining the transport properties of the films on sapphire substrates. In the case of LSMO:ZnO films on LAO substrates, TEM results show that the microstructure does not change with film thickness in the nanocomposite films (Figure 2e). Thus, the T_{MI} and resistivity variation with the film thickness could be correlated with the strain effect.

Discussion

In order to fit the magnetotransport results in the whole temperature range, including the abnormal high resistance at low temperatures (see Figures 3a and 3b), a modified parallel connection channel model was used (see supporting information V) to analyze the experimental results^{47,48},

$$\frac{1}{\rho} = \frac{S_i}{\rho_i} + \frac{S_m}{\rho_{LSMO} + \rho_{cb}} \quad (1)$$

(ρ_{LSMO} in series with ρ_{cb} when films are thin)

$$\frac{1}{\rho} = \frac{S_i}{\rho_i} + \frac{S_m}{\rho_{LSMO}} + \frac{S_{cb}}{\rho_{cb}} \quad (2)$$

(ρ_{LSMO} in parallel with ρ_{cb} when films are thick)

where ρ_i and ρ_{LSMO} denote the resistivity for insulating and conducting channels, respectively. ρ_{cb} represents the contribution from the Coulomb blockade effect⁴⁸. S_i , S_m , S_{cb} are the effective cross-sections of these channels. The geometrical factor (G) is defined as $G = S_i/S_m$. A thermally activated conduction mechanism was used to simulate the insulating channel with $\rho_i = \exp(\Delta E_i/k_B T)$. ΔE_i is the effective activation energy for the insulating phase, k_B is Boltzmann's constant and T is the absolute temperature. For simplicity, the resistivity of

LSMO is determined by the ferromagnetic (FM) domains with $\rho_{LSMO} = \rho_0 + aT^{2.5} + bT^{5.49,50}$. The first term ρ_0 corresponds to the residual resistivity arising from defect and impurity scattering. The second and third terms represent the electron-electron and electron-phonon scattering, respectively. Coulomb blockade effect was simulated by thermal activated conduction mechanism with $\rho_{cb} = A \exp(\Delta E_a/k_B T)$ where A is an amplitude factor and ΔE_a is the very small effective activation energy for the disordered GBs activated only at temperatures lower than 50 K⁴⁸. The detailed fitting results are shown in Tables SI and SII. It is very interesting to note that the geometrical factor in these two systems is quite different (Figure 3f). The G factor of the nanocomposites grown on *r*-plane sapphire increases gradually with decreasing film thickness, while that of the nanocomposite films deposited on *c*-plane sapphire is almost independent of the film thickness (Figure 3f). The results are consistent with the microstructure variations of the nanostructures on sapphire substrates. The phenomenological model is not suitable for the thin nanocomposite films on LAO substrates since the large strain effect can significantly alter the FM behavior of the LSMO phase.

Temperature dependence of MR is shown in Figure 4. It can be seen that the MR of nanocomposite films on *r*-plane sapphire substrates depends strongly on film thickness. The MR of thin samples (e.g. 20 nm and 35 nm) decreases with the increase of temperature. The large MR at low temperatures is induced by the GB or the phase boundary, which is consistent with the small grain structure and high density of GBs observed in Figures 2b and 3e. With increasing film thickness, the nanocomposite films behave as the conventional FM LSMO where the low temperature MR induced by boundaries is dramatically reduced. This observation is consistent with the large LSMO grains and significantly reduced GB density and resistivity (Figures 2a and 3e). As the strain effect in LSMO:ZnO on sapphire is ruled out, the evolution of microstructure (Figure 2) as a function of film thickness plays an important role in determining the transport properties of the films. Figure 4b reveals that the MR of the nano-

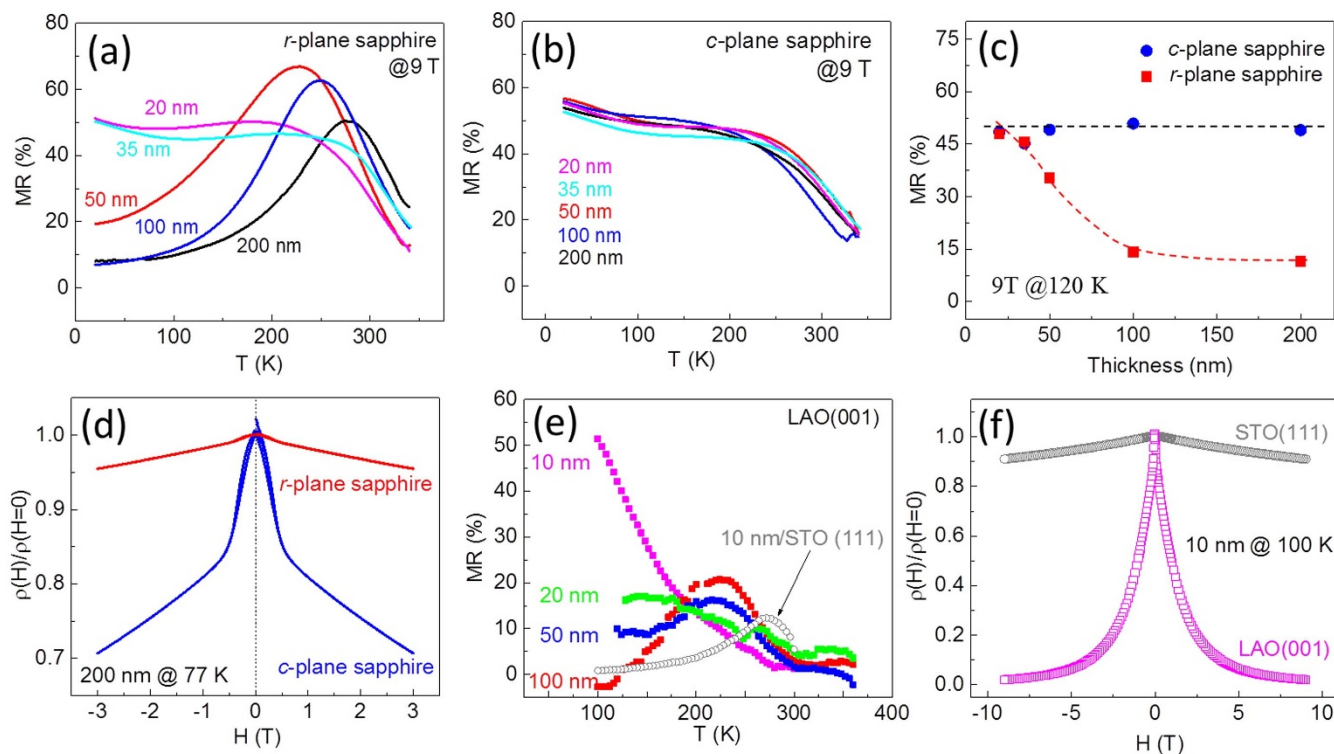


Figure 4 | MR of LSMO:ZnO nanocomposite films. (a) and (b) Temperature dependent MR (9 T) of LSMO:ZnO films with different thicknesses on *r*- and *c*-plane sapphires, respectively. (c) MR (120 K) vs. film thickness. (d) Field dependent MR (77 K) of 200 nm nanocomposite films on *r*-plane sapphire and *c*-plane sapphire. (e) Temperature dependent MR (1 T) of LSMO:ZnO films on LAO (001) with different thicknesses. The reference sample (10 nm nanostructure on STO (111)) is also shown. (f) Field dependent MR (100 K) of 10 nm nanocomposite films on LAO (001) and on STO (111).

composite films on *c*-plane sapphire with different thicknesses is almost the same. The significant low temperature MR, independent of film thickness (Figure 4c), indicates that high density GBs exist along the conducting paths, which is evidenced by the extremely large low temperature resistivity (Figure 3e). The low temperature MR of samples on *r*- and *c*-plane sapphires is compared in Figure 4c. Similar behaviors including $R(T)$ and $MR(T)$ are observed in these thin films (e.g. 20 nm) on sapphire substrates (Figures 3 and 4). There is a large discrepancy in MR of thick films. For instance, the MR of 200 nm nanocomposite films on *c*-plane sapphire is ~49%, which is much larger than that of ~11% for the film on *r*-plane sapphire with the same thickness. $R(H)$ curves at 77 K show that the low-field MR exists in the films on *c*-plane sapphire, suggesting the boundaries are along the electron conducting path (Figure 4d). In contrast, the much smaller low-field MR for the film on *r*-plane sapphire indicates lower density of GBs, at least the boundaries are not dominating factors in controlling the electron conduction. Figure 4e shows the MR of nanocomposite films grown on LAO (001). A very large MR was observed for the films thinner than 50 nm. For instance, a MR of 50% was observed in a 10 nm film at 1 T and 100 K. When the films become thicker, the low temperature MR decreases dramatically. The thickness dependence of MR and resistivity can be explained by the strain effect. When the nanocomposite films are thin enough, the epitaxial strain induced by the substrate controls the transport behaviors. Since the lattice constant of LAO is smaller than that of LSMO, LSMO phase is in tension out-of-plane. The $M-H$ measurements show that thick films (e.g. 200 nm) exhibit an in-plane easy axis due to the large demagnetization field (not shown here). However, the thinner film (50 nm) reveals an out-of-plane easy axis (Figure S7). XRD results shown in Figure 1 indicate that the strain of LSMO phase in the 10 nm (50 nm) film is as large as 2.8% (1.3%). This tensile strain may enable magnetic moments to overcome the demagnetization field and result

in the magnetic spins aligned out-of-plane⁵¹. The spin up and down configured magnetic domains, induced by tensile strain, can lead to much enhanced MR in epitaxial films⁵¹. As the nanocomposite films become thicker, the epitaxial strain from the substrate reduces and so does the low temperature MR. For comparison, the LSMO phase in the LSMO:ZnO on STO (111) with a compressive strain of -0.9% shows negligible low-field MR at low temperatures (Figure 4e). Figure 4f shows the field dependent resistivity ratio ρ_H/ρ_0 of 10 nm LSMO:ZnO films on both LAO and SrTiO₃ (111) substrates at 100 K. A 2.8% strain in the 10 nm nanocomposite film on LAO can lead to a MR of almost 100% at a magnetic field of 9 T, which is much larger than that of samples on STO (111) with 0.9% strain. The highly strained nanocomposite films exhibit much enhanced MR compared to the similar nanocomposites with lower strain effect, indicating that strain is the dominating effect in nanocomposites grown on LAO substrates.

In summary, film thickness plays an important role in tuning the physical properties of LSMO:ZnO nanocomposite films. By using XRD and TEM, we have carefully analyzed thickness dependent strain and microstructures. The magnetotransport properties of the nanocomposite films have been fitted by a modified parallel connection channel model, in agreement with the change of microstructure in nanocomposite films on sapphire substrates. The strain analysis indicates that the variation of physical properties in nanocomposite films on LAO is dominated by the strain. These results emphasize the significant effect of film thickness on microstructures, strain states, and functionalities. This work further illustrates that functionalities can be manipulated by using nanocomposite films with variable thicknesses.

Methods

Thin Film Growth. LSMO:ZnO nanocomposite films with different thicknesses (10 nm to 200 nm) were grown on *r*-plane sapphire, *c*-plane sapphire, and LAO (001) by using pulsed laser deposition (PLD) with a KrF excimer laser (Lambda Physik LPX



300, $\lambda = 248$ nm, 2 Hz). The composite target used for the deposition was fabricated by a conventional ceramic sintering process. The rectangle laser beam with an area of 5.55 mm^2 was focused onto the composite target with an energy density of 2.0 J/cm^2 . Prior to the deposition, the chamber was pumped to a base pressure of 1.0×10^{-6} Torr. A substrate temperature of 750°C and an oxygen pressure of 100 mTorr were maintained during the depositions. Both the target and the substrate are rotated during the deposition to achieve better uniformity. The deposition rate of the films is $\sim 0.4 \text{ \AA/pulse}$. After deposition, the films were cooled down to room temperature at $10^\circ\text{C min}^{-1}$ in an oxygen pressure of 250 Torr.

Microstructural Characterization. The orientation of the nanocomposite films was investigated by XRD (Panalytical MRD PRO X-ray diffractometer). The microstructure was characterized by TEM and STEM-EDX (FEI Tecnai F30 analytical TEM operating at 300 kV).

Magnetic and Magnetotransport Measurements. Au electrodes deposited by sputtering were used for the magnetotransport measurements. The electrical properties of the films at temperatures from 20 K to 360 K and a magnetic field up to 9 T were measured using a commercial Physical Properties Measurement System (Quantum Design, PPMS). Before magnetization and magnetotransport measurements, all samples were thermally demagnetized. During the magnetotransport measurements, the magnetic field was applied perpendicular to the film plane and the current was applied along the in-plane of the film. The in-plane and out-of-plane magnetizations vs. field ($M \sim H$) were also measured by applying a magnetic field parallel and perpendicular to the film plane, respectively. Before the measurement of magnetization vs. temperature ($M \sim T$) characteristics, films were zero field cooled (ZFC) or field cooled (FC) at 500 Oe from 360 K to 5 K. $M \sim T$ curves were subsequently recorded during the heating from 5 K to 360 K under zero field.

- Norton, D. P. *et al.* Superconductivity in SrCuO₂-BaCuO₂ Superlattices - Formation of artificially layered superconducting materials. *Science* **265**, 2074–2077 (1994).
- Prellier, W., Singh, M. P. & Murugavel, P. The single-phase multiferroic oxides: from bulk to thin film. *J. Phys.-Condens. Mat.* **17**, R803–R832 (2005).
- Martin, L. W. & Schlom, D. G. Advanced synthesis techniques and routes to new single-phase multiferroics. *Curr. Opin. Solid. St. M.* **16**, 199–215 (2012).
- Chen, A. P. *et al.* A new class of room-temperature multiferroic thin films with Bismuth-based supercell structure. *Adv. Mater.* **25**, 1028–1032 (2013).
- Visser, D. W., Ramirez, A. P. & Subramanian, M. A. Thermal conductivity of manganite perovskites: Colossal magnetoresistance as a lattice-dynamics transition. *Phys. Rev. Lett.* **78**, 3947–3950 (1997).
- Subramanian, M. A. *et al.* Colossal magnetoresistance without Mn³⁺/Mn⁴⁺ double exchange in the stoichiometric pyrochlore Ti₂Mn₂O₇. *Science* **273**, 81–84 (1996).
- Pantel, D., Goetze, S., Hesse, D. & Alexe, M. Reversible electrical switching of spin polarization in multiferroic tunnel junctions. *Nat. Mater.* **11**, 289–293 (2012).
- Murakami, M. *et al.* Tunable multiferroic properties in nanocomposite PbTiO₃-CoFe₂O₄ epitaxial thin films. *Appl. Phys. Lett.* **87**, 112901 (2005).
- Laukhin, V. *et al.* Electric-field control of exchange bias in multiferroic epitaxial heterostructures. *Phys. Rev. Lett.* **97**, 227201 (2006).
- Levin, I., Li, J. H., Slutsker, J. & Roytburd, A. L. Design of self-assembled multiferroic nanostructures in epitaxial films. *Adv. Mater.* **18**, 2044–2047 (2006).
- Zhu, Y. M. *et al.* Self-assembled perovskite-spinel heterostructure on a highly distorted substrate. *Appl. Phys. Lett.* **102**, 111903 (2013).
- Liu, H. J. *et al.* Epitaxial photostriction-magnetostriction coupled self-assembled nanostructures. *ACS Nano* **6**, 6952 (2012).
- Wee, S. H. *et al.* Self-assembly of nanostructured, complex, multication films via spontaneous phase separation and strain-driven ordering. *Adv. Funct. Mater.* **23**, 1912–1918 (2013).
- Liu, H. J. *et al.* Large magnetoresistance in magnetically coupled SrRuO₃-CoFe₂O₄ self-assembled nanostructures. *Adv. Mater.* **25**, 4753–4759 (2013).
- Khatkhatay, F. *et al.* Ferroelectric properties of vertically aligned nanostructured BaTiO₃-CeO₂ thin films and their integration on Silicon. *ACS Appl. Mater. Inter.* **5**, 12541–12547 (2013).
- Ning, X. K., Wang, Z. J., Zhao, X. G., Shih, C. W., Chang, W. C. & Zhang, Z. D. Exchange bias effect and magnetic properties in La_{0.7}Sr_{0.3}MnO₃-NiO nanocomposite films. *IEEE T. Magn.* **50**, 1000304 (2014).
- Liao, X. B., Ni, Y., Yang, H. & He, L. H. Role of modulus mismatch in vertically aligned nanocomposite formation during spinodal decomposition in constrained films. *Appl. Phys. Lett.* **103**, 141903 (2013).
- Lee, O. *et al.* Extremely high tunability and low Loss in nanoscaffold ferroelectric films. *Nano Lett.* **12**, 4311–4317 (2012).
- Aimon, N. M., Kim, D. H., Choi, H. K. & Ross, C. A. Deposition of epitaxial BiFeO₃/CoFe₂O₄ nanocomposites on (001) SrTiO₃ by combinatorial pulsed laser deposition. *Appl. Phys. Lett.* **100**, 092901 (2012).
- MacManus-Driscoll, J. L. *et al.* Strain control and spontaneous phase ordering in vertical nanocomposite heteroepitaxial thin films. *Nat. Mater.* **7**, 314–320 (2008).
- Chen, A. P., Bi, Z. X., Jia, Q. X., MacManus-Driscoll, J. L. & Wang, H. Y. Microstructure, vertical strain control and tunable functionalities in self-assembled, vertically aligned nanocomposite thin films. *Acta Mater.* **61**, 2783 (2013).
- Zheng, H. *et al.* Multiferroic BaTiO₃-CoFe₂O₄ nanostructures. *Science* **303**, 661–663 (2004).

- Ryu, H. *et al.* Magnetoelectric effects of nanoparticulate Pb(Zr_{0.52}Ti_{0.48})O₃-NiFe₂O₄ composite films. *Appl. Phys. Lett.* **89**, 102907 (2006).
- Tan, Z. P., Slutsker, J. & Roytburd, A. L. Epitaxial self-assembly of multiferroic nanostructures. *J. Appl. Phys.* **105**, 061615 (2009).
- Oh, Y. S. *et al.* Quantitative determination of anisotropic magnetoelectric coupling in BiFeO₃-CoFe₂O₄ nanostructures. *Appl. Phys. Lett.* **97**, 052902 (2010).
- Yan, L. *et al.* Direct measurement of magnetoelectric exchange in self-assembled epitaxial BiFeO₃-CoFe₂O₄ nanocomposite thin films. *Appl. Phys. Lett.* **94**, 192902 (2009).
- Hsieh, Y. H. *et al.* Local conduction at the BiFeO₃-CoFe₂O₄ tubular oxide interface. *Adv. Mater.* **24**, 4564–4568 (2012).
- Su, Q. *et al.* Vertically aligned nanocomposite electrolytes with superior out-of-plane ionic conductivity for solid oxide fuel cells. *J. Power Sources* **242**, 455–463 (2013).
- Dix, N. *et al.* Selectable spontaneous polarization direction and magnetic anisotropy in BiFeO₃-CoFe₂O₄ epitaxial nanostructures. *ACS Nano* **4**, 4955–4961 (2010).
- Tsai, C. Y. *et al.* Stress-mediated magnetic anisotropy and magnetoelastic coupling in epitaxial multiferroic PbTiO₃-CoFe₂O₄ nanostructures. *Appl. Phys. Lett.* **102**, 132905 (2013).
- Zhang, W. *et al.* Strain relaxation and enhanced perpendicular magnetic anisotropy in BiFeO₃:CoFe₂O₄ vertically aligned nanocomposite thin films. *Appl. Phys. Lett.* **104**, 062402 (2014).
- Fix, T. *et al.* Electric-field control of ferromagnetism in a nanocomposite via a ZnO phase. *Nano Lett.* **13**, 5886–5890 (2013).
- Schmitz-Antoniak, C. *et al.* Electric in-plane polarization in multiferroic CoFe₂O₄/BaTiO₃ nanocomposite tuned by magnetic fields. *Nat. Commun.* **4**, 2051 (2013).
- Brassard, D., Fourmaux, S., Jean-Jacques, M., Kieffer, J. C. & El Khakani, M. A. Grain size effect on the semiconductor-metal phase transition characteristics of magnetron-sputtered VO₂ thin films. *Appl. Phys. Lett.* **87**, 051910 (2005).
- Bollero, A. *et al.* Influence of thickness on microstructural and magnetic properties in Fe₃O₄ thin films produced by PLD. *J. Magn. Magn. Mater.* **285**, 279–289 (2005).
- Dong, B. Z., Fang, G. J., Wang, J. F., Guan, W. J. & Zhao, X. Z. Effect of thickness on structural, electrical, and optical properties of ZnO:Al films deposited by pulsed laser deposition. *J. Appl. Phys.* **101**, 033713 (2007).
- Shim, E. S., Kang, H. S., Kang, J. S., Kim, J. H. & Lee, S. Y. Effect of the variation of film thickness on the structural and optical properties of ZnO thin films deposited on sapphire substrate using PLD. *Appl. Surf. Sci.* **186**, 474–476 (2002).
- Kale, S. *et al.* Film thickness and temperature dependence of the magnetic properties of pulsed-laser-deposited Fe₃O₄ films on different substrates. *Phys. Rev. B* **64**, 205413 (2001).
- Moshnyaga, V. *et al.* Structural phase transition at the percolation threshold in epitaxial (La_{0.7}Ca_{0.3}MnO₃)_{1-x}MgO_x nanocomposite films. *Nat. Mater.* **4**, 247–252 (2005).
- Chen, A. P. *et al.* Magnetotransport properties of quasi-one-dimensionally channelled vertically aligned heteroepitaxial nanomazes. *Appl. Phys. Lett.* **102**, 093114 (2013).
- Zheng, H. M. *et al.* Self-assembled growth of BiFeO₃-CoFe₂O₄ nanostructures. *Adv. Mater.* **18**, 2747–2752 (2006).
- Bi, Z. X. *et al.* Microstructural and magnetic properties of (La_{0.7}Sr_{0.3}MnO₃)_{0.7}(Mn₃O₄)_{0.3} nanocomposite thin films. *J. Appl. Phys.* **109**, 054302 (2011).
- Chen, A. P. *et al.* Microstructure, magnetic, and low-field magnetotransport properties of self-assembled (La_{0.7}Sr_{0.3}MnO₃)_{0.5}(CeO₂)_{0.5} vertically aligned nanocomposite thin films. *Nanotechnology* **22**, 315712 (2011).
- Mohaddes-Ardabili, L. *et al.* Size and shape evolution of embedded single-crystal alpha-Fe nanowires. *Appl. Phys. Lett.* **87**, 203110 (2005).
- Zhang, W. R. *et al.* Integration of self-assembled vertically aligned nanocomposite (La_{0.7}Sr_{0.3}MnO₃)_{1-x}ZnO_x thin films on silicon substrates. *ACS Appl. Mater. Inter.* **5**, 3995–3999 (2013).
- Dix, N. *et al.* Critical limitations in the fabrication of biferric BiFeO₃-CoFe₂O₄ columnar nanocomposites due to bismuth loss. *Chem. Mater.* **21**, 1375–1380 (2009).
- Chen, A. P. *et al.* Tunable low-field magnetoresistance in (La_{0.7}Sr_{0.3}MnO₃)_{0.5}(ZnO)_{0.5} self-assembled vertically aligned nanocomposite thin films. *Adv. Funct. Mater.* **21**, 2423–2429 (2011).
- de Andres, A., Garcia-Hernandez, M. & Martinez, J. L. Conduction channels and magnetoresistance in polycrystalline manganites. *Phys. Rev. B* **60**, 7328–7334 (1999).
- Schiffer, P., Ramirez, A. P., Bao, W. & Cheong, S. W. Low-temperature magnetoresistance and the magnetic phase-diagram of La_{1-x}Ca_xMnO₃. *Phys. Rev. Lett.* **75**, 3336–3339 (1995).
- Boschker, H. *et al.* Optimized fabrication of high-quality La_{0.67}Sr_{0.33}MnO₃ thin films considering all essential characteristics. *J. Phys. D. Appl. Phys.* **44**, 205001 (2011).
- Wang, H. S., Li, Q., Liu, K. & Chien, C. L. Low-field magnetoresistance anisotropy in ultrathin Pr_{0.67}Sr_{0.33}MnO₃ films grown on different substrates. *Appl. Phys. Lett.* **74**, 2212–2214 (1999).

Acknowledgments

This work was supported by the U.S. DOE through the NNSA's Laboratory Directed Research and Development Program and performed, in part, at the Center for Integrated



Nanotechnologies (CINT), a U.S. DOE, Office of Basic Energy Sciences user facility. Los Alamos National Laboratory, an affirmative action equal opportunity employer, is operated by Los Alamos National Security, LLC, for the National Nuclear Security Administration of the U.S. DOE under Contract DE-AC52-06NA25396. J.L.M.-D thanks the ERC for the Advanced Investigator Grant, Novox, ERC-2009-adG 247276 and the EPSRC (U.K.) for grant EP/H047867/1. The effort at Texas A&M University is supported by the U.S. National Science Foundation (DMR-1401266, 1007969 and 0846504).

Author contributions

A.C., Z.B. and Q.X.J. designed and implemented the experiments. A.C., Z.B., X.L. and P.D. carried out the thin film growth. A.C. and Z.B. characterized the microstructure. M.W. performed the magnetotransport measurements. W.Z. and H.W. carried out part of the XRD measurements. A.C. interpreted the data and drafted the manuscript. H.W., J.M. and Q.X.J. revised the manuscript. All authors discussed the results and commented on the manuscript.

Additional information

Supplementary information accompanies this paper at <http://www.nature.com/scientificreports>

Competing financial interests: The authors declare no competing financial interests.

How to cite this article: Chen, A.P. *et al.* Evolution of microstructure, strain and physical properties in oxide nanocomposite films. *Sci. Rep.* 4, 5426; DOI:10.1038/srep05426 (2014).



This work is licensed under a Creative Commons Attribution-NonCommercial-ShareAlike 4.0 International License. The images or other third party material in this article are included in the article's Creative Commons license, unless indicated otherwise in the credit line; if the material is not included under the Creative Commons license, users will need to obtain permission from the license holder in order to reproduce the material. To view a copy of this license, visit <http://creativecommons.org/licenses/by-nc-sa/4.0/>